IRAS 12553–7651 in Chamaeleon II: a low mass PMS star with a C^{18}O outflow?[*]

L. Olmi[1]**, M. Felli**[2]**, and R. Cesaroni**[2]

[1] Cornell University, Arecibo Observatory, P.O. Box 995, Arecibo, 00613, Puerto Rico[**]
[2] Osservatorio Astrofisico di Arcetri, Largo E. Fermi 5, I-50125 Firenze, Italy

Abstract. We present new multi-line, multi-isotope observations of the PMS candidate IRAS 12553–7651 in the nearby Chamaeleon II dark cloud. Previous far infrared and molecular observations towards three selected objects in Cha II determined that IRAS 12553–7651 was the most likely candidate to be a young (proto)stellar object. We thus mapped the IRAS 12553–7651 region in the ^{12}CO $J = 2 \rightarrow 1$, ^{13}CO $J = 2 \rightarrow 1$, and C^{18}O $J = 1 \rightarrow 0$ rotational transitions to use probes more sensitive to higher density gas and not affected by optical depth effects. We also observed and detected the C^{34}S $J = 2 \rightarrow 1$ transition. Our observations confirm the presence of a high-density clump at the position of the IRAS source with $V_{\mathrm{LSR}} \simeq 3$ km s^{-1}, and reveal a C^{18}O *velocity shift* aligned along an axis SW-NE, of about 2 km s^{-1} pc^{-1}, which is likely to be an outflow. Based upon this assumption, the ^{13}CO spectra of Olmi et al. (1994) have been re-analyzed and found to show a deviation from a Gaussian shape. This asymmetry can be interpreted in terms of a line component which migrates in velocity with respect to the ambient cloud. We show that a model in which the bipolar outflow interacts with the ambient gas around IRAS 12553–7651 may reproduce qualitatively the observational data.

Key words: interstellar medium: clouds: Chamaeleon II – interstellar medium: molecules – radio lines: interstellar

1. Introduction

The Chamaeleon complex is one of the low-mass star forming regions and molecular clouds (Olmi et al. 1994, hereafter OFP) closest to the Sun. It is located at $\alpha \simeq 13^{\mathrm{h}}$, $\delta \simeq -77°$, and contains three main dark clouds: Cha I, II, and III. We concentrate here on Chamaeleon II, located at a distance of 180 ± 20 pc

(Whittet et al. 1991), and which is probably in an earlier phase of evolution than Cha I (Prusti et al. 1992).

IRAS 12553–7651 (hereafter I12553) is a low-luminosity object (1.2 $L_{\odot}$), which is likely to be a warm embedded source. In fact, (i) it has been detected at all IRAS wavelengths and classified as a warm, embedded object (Prusti et al. 1992), (ii) a compact ^{13}CO clump is found around the IRAS source, (iii) CS emission appears to come from roughly the same region, although at a velocity different from that of the compact ^{13}CO, and (iv) a comparison of the mass as estimated from the column density and the virial theorem suggests that the "compact" component is not in gravitational equilibrium. From star counts the total visual extinction towards Cha II turns out to be about 5 magnitudes towards I12553 (Gregorio Hetem et al. 1988, 1989). I12553 was not detected by Henning et al. (1993) at $\lambda = 1.3$ mm to a level of 50 mJy. With a lack of NIR and sub-mm data it is difficult to classify the source by its spectral energy distribution (SED). However, the upper limit at 1.3 mm, and the detection by IRAS at all wavelengths seem to suggest a low circumstellar dust content and therefore a more evolved object than Class I source (see, e.g., Lada 1991).

OFP observed a ^{13}CO "compact" condensation at $V_{\mathrm{LSR}} \simeq 1$ km s^{-1} close to the IR source. A comparison of the mass as estimated from the column density and from the virial theorem suggests that the "compact" component at $V_{\mathrm{LSR}} \simeq 1$ km s^{-1} is not in gravitational equilibrium. CS $J = 2 \rightarrow 1$ emission was detected at the position of the IR source, but at ~ 3 km s^{-1}. The upper limit for the hydrogen number density was a few times 10^4 cm^{-3}, although this estimate was based on just a single rotational transition of CS and thus needed a further study using the rare isotope C^{34}S.

One major difficulty in studying individual molecular clumps in the Cha II region is the intense ^{12}CO and ^{13}CO emission over a very extended region. As ^{12}CO is optically thick, a multi-transition, multi-isotope study was needed, using both CO and CS molecules, to study smaller and denser clumps inside the large molecular cloud. However, ^{13}CO is subject to complex fractionation effects, while C^{18}O is a superior probe of the physical conditions deep inside the cloud.

Sect. 2 of this paper gives a detailed description of the new observations carried out with the ESO-SEST telescope, which include optically thin transitions, such as the $C^{18}O$ $J = 1 \rightarrow 0$, ^{13}CO $J = 2 \rightarrow 1$ and $C^{34}S$ $J = 2 \rightarrow 1$ lines.

Sect. 3 presents an overview of the main results obtained. In particular, we find a small $C^{18}O$ clump at $V_{LSR} \simeq 3$ km s^{-1} associated with the IR source. The $C^{18}O$ emission presents a SW-NE velocity shift measured in the $C^{18}O$ map at $V_{LSR} \simeq 3$ km s^{-1}, which is *not* observed in the other molecular tracers. No $C^{18}O$ counterpart, up to a 3σ level of ~ 0.09 K, is seen at the velocity ($V_{LSR} \simeq 1$ km s^{-1}) of the $^{13}CO(1-0)$ "compact" component discussed by OFP.

In Sect. 4, we describe the various cloud components, discussing in particular the line asymmetry at $V_{LSR} \simeq 3$ km s^{-1} found in the $^{13}CO(1-0)$ and, to some extent, also in the $^{13}CO(2-1)$ spectra. We then present a detailed analysis of the ^{12}CO and ^{13}CO observations in terms of excitation temperature, optical depth, and filling factors.

In Sect. 5 we concentrate our attention on the "compact" clump at ~ 1 km s^{-1}. We review the emission found by OFP in the $^{13}CO(1-0)$ rotational transition, adding new insights from the $^{12}CO(2-1)$ observations and calculating the clump mass.

Sect. 6 describes the velocity shift measured in the $C^{18}O(1-0)$ line at ~ 3 km s^{-1}, interpreted as a bipolar outflow. Based on these findings we then discuss the central source of energy associated with I12553.

The departure from a Gaussian shape in the ^{13}CO component at ~ 3 km s^{-1} is described in Sect. 7. We present a simple geometrical model for the interaction of the outflowing gas from I12553 with the surrounding molecular material, which can qualitatively reproduce the observed line profiles. Finally, in Sect. 8, we summarize our conclusions.

2. Observations and data reduction

2.1. System parameters

The observations were carried out using the 15-m Swedish-ESO Submillimetre Telescope[1] (Booth et al. 1989), at the European Southern Observatory, La Silla, Chile, in January 1995. A complete list of the molecular lines observed and the system parameters is given in Table 1.

The 3 mm dual-polarization receivers employed cooled Schottky barrier diode mixers, whereas the λ=1.3 mm single-polarization receiver used a cooled SIS mixer. The backend was a high resolution acousto-optical spectrometer (AOS) with a total bandwidth of 86 MHz and a channel separation of 43 kHz. The observations were made in both frequency-switched (with a 10 MHz throw) and position-switched modes (the reference position $\alpha = 13^h04^m$, $\delta = -76°$ was checked for absence of emission). Given the quasi-optical arrangement of the secondary focus at SEST, we used the two channels of the 3 mm receiver
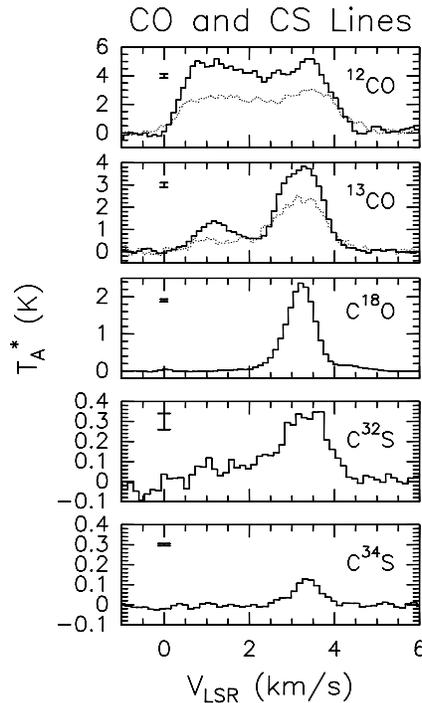
Fig. 1. Spectra of the observed CO and CS lines toward the central position of I12553. From top to bottom: ^{12}CO, ^{13}CO, $C^{18}O$, $C^{32}S(2-1)$, and $C^{34}S(2-1)$. In the case of CO, solid and dotted lines correspond respectively to (1–0) and (2–1) transitions. Typical 1σ RMS noise is shown with an error bar in the upper left-hand corner of the plots

to observe ^{12}CO and $C^{18}O$ (in position-switched modes) simultaneously. The data were calibrated using the standard chopper-wheel technique, and therefore the spectra are on the T_a^* scale (Kutner and Ulich 1981). The temperature scale was then converted to main beam brightness temperature, T_{MB}, by dividing T_a^* by the main beam efficiencies ($\eta_{MB} = 0.7$ at 115 GHz and 0.6 at 230 GHz). Most of the lines were observed on two contiguous days, and the weather changes during the run resulted in about a 9% ($C^{18}O$) and 13% ($^{13}CO[2-1]$) internal calibration uncertainty.

In the following, all positions are given in arcsec offsets with respect to I12553 ($\alpha[1950] = 12^h55^m20.3^s$, $\delta[1950] = -76°51'22''$). The pointing was regularly checked during the observing run by means of spectral line observations of SiO (v=1, $J=2-1$) masers. Repeated observations of selected positions within the region around I12553, resulted in a pointing uncertainty of $< 8''$. Integration times, split into several chunks to reduce instabilities effects in the AOS, varied from 1 (^{12}CO) to 30 ($C^{34}S$) min, and consequently sensitivities varied between 0.4 and 0.04 K (on the T_a^* scale). During data reduction with the CLASS package, the frequency-switched spectra were folded in frequency and polynomial baselines fitted and removed.

Table 1. List of molecular lines observed towards IRAS 12553–7651, and some instrumental parameters, including the integration time, Δt, and the RMS antenna temperature level, ΔT_a^*

Transition	Rest Frequency (GHz)	Velocity Resolution (km/s)	Beam FWHM (arcsec)	T_{sys} (K)	Δt (min)	ΔT_a^* (K)
$C^{34}S\ J = 2 \rightarrow 1$[a]	96.41298	0.13	53	360-390	15-30	0.04-0.06
$C^{18}O\ J = 1 \rightarrow 0$	109.78218	0.12	47	360-590	1-10	0.05-0.15
$^{13}CO\ J = 2 \rightarrow 1$	220.39869	0.059	24	780-1100	1-10	0.1-0.4
$^{12}CO\ J = 2 \rightarrow 1$	230.53799	0.056	23	560-1050	1	0.2-0.4

[a] observed towards the center only

Table 2. Observed line parameters toward the central (0,0) position. Errors are formal 1σ values and do not take into account the calibration uncertainty. The $^{13}CO(1–0)$ and $C^{32}S(2–1)$ data are from OFP

Line	Component	V_{LSR} (km s^{-1})	FWHM (km s^{-1})	FWFN[a] (km s^{-1})	T_a^* (K)
$^{12}CO(2–1)$	–	2.2 ± 0.1[b]	3.8 ± 0.1	5.6 ± 0.1	3.1 ± 0.2[c]
$^{13}CO(2–1)$	$[1^{st}]$[d]	1.1 ± 0.1	0.9 ± 0.1		0.6 ± 0.1
$^{13}CO(2–1)$	$[2^{nd}]$[d]	3.2 ± 0.1	1.4 ± 0.1		2.5 ± 0.1
$C^{18}O(1–0)$	–	3.2 ± 0.1	0.8 ± 0.1	3.9 ± 0.3	2.3 ± 0.1
$^{13}CO(1–0)$[e]	$[1^{st}]$[f]	1.3 ± 0.1	1.2 ± 0.1		1.3 ± 0.1
$^{13}CO(1–0)$[e]	$[2^{nd}]$[f]	2.7 ± 0.1	0.5 ± 0.1		1.2 ± 0.1
$^{13}CO(1–0)$[e]	$[3^{rd}]$[f]	3.3 ± 0.1	1.0 ± 0.1		3.8 ± 0.1
$C^{32}S(2–1)$[e]	–	3.3 ± 0.1	0.9 ± 0.1		0.3 ± 0.1
$C^{34}S(2–1)$	–	3.4 ± 0.1	0.7 ± 0.1		0.13 ± 0.01

[a] Full Width at First Nulls
[b] Average velocity in the range of emission
[c] Peak antenna temperature
[d] Result of a 2-, rather than 3-component, Gaussian fit, because of a low signal-to-noise ratio
[e] As observed by OFP
[f] Result of a 3-component Gaussian fit (see Sect. 4.1)

3. Results

3.1. $^{12}CO(2–1)$

Spectra of the $^{12}CO(2–1)$ line were taken on 94 positions at spacings between $20''$ and $80''$, and covering a total area of approximately $6'.7 \times 6'.7$. The $^{12}CO(2–1)$ map was therefore quite undersampled, but the main purpose of the observation was to obtain the large-scale distribution of the molecular gas around I12553. The observations indicate that $^{12}CO(2–1)$ is both optically thick and extended. The $^{12}CO(2–1)$ spectrum at (0,0), as well as of the other lines, are shown in Fig. 1. We also include the $^{12}CO(1–0)$ and $^{13}CO(1–0)$ lines observed by OFP. Table 2 shows the main observed line parameters toward the central position.

The spatial distribution of the $^{12}CO(2–1)$ emission is shown in Fig. 2. The emission is smooth, with no particular features at velocities ≥ 2 km s^{-1}. In contrast, at $V_{LSR} \leq 2$ km s^{-1} one clearly sees that the emission is concentrated towards an elongated clump laying $\sim 40''$ from the nominal position of I12553. We do not detect any evident line-wing (at an RMS level of $\Delta T_a^* \simeq 0.3$ K; this and the following noise estimates

are given in terms of the antenna temperature scale unless otherwise stated) at the position of I12553.

3.2. $^{13}CO(2–1)$

Our $^{13}CO(2–1)$ maps were made of 47 positions at sampling intervals of $40''$ and $60''$, and covering a total area of approximately $4'.7 \times 4'.7$, symmetrically placed around the position of I12553. Our spectra have a low signal-to-noise ratio (SNR), and therefore they do not show the typical two velocity components of the $^{13}CO(1–0)$ spectra. However, when summing spectra from adjacent positions the weak component at $V_{LSR} \simeq 1$ km s^{-1} shows up, and a 2-component Gaussian fit is possible. Furthermore, using this technique, one can reveal deviations of the "main" component at $V_{LSR} \simeq 3$ km s^{-1} from a Gaussian line profile, similar to those observed in the $^{13}CO(1–0)$ line (see Sect. 4.1).

The $^{13}CO(2–1)$ emission bot at ~ 1 and ~ 3 km s^{-1} is more concentrated in a single spatial component than $^{12}CO(2–1)$. This is shown in the maps of the integrated intensity (Fig. 3), where
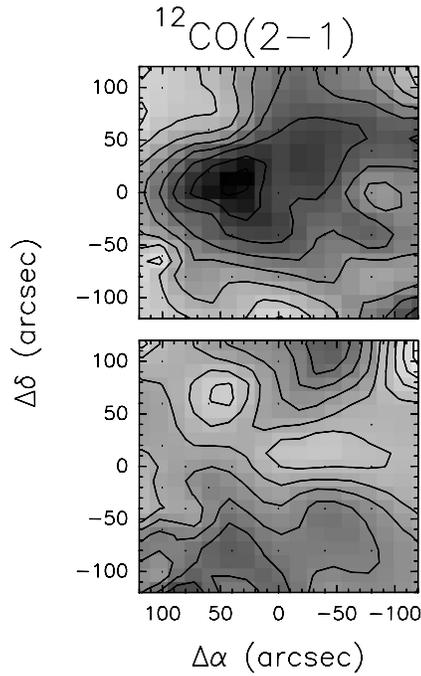
Fig. 2. *Top*: map of the ^{12}CO(2–1) integrated antenna temperature, $\int T_a^* dv$, from -0.15 to 2.0 km s^{-1}. The lowest contour level is 1.8 K km s^{-1} and the interval between adjacent contours is 0.3 K km s^{-1}. The black dots indicate the positions where data were taken. *Bottom*: same as above for the range 2.5 to 5.0 km s^{-1}. The lowest contour level is 3.0 K km s^{-1} and the interval between adjacent contours is 0.3 K km s^{-1}

Fig. 3. *Top*: map of the ^{13}CO(2–1) integrated antenna temperature, from 0.2 to 2.0 km s^{-1}. The lowest contour level is 0.3 K km s^{-1} and the interval between adjacent contours is 0.2 K km s^{-1}. The black dots indicate the positions where data were taken. *Bottom*: same as above for the range 2.2 to 4.3 km s^{-1}. The lowest contour level is 1.6 K km s^{-1} and the interval between adjacent contours is 0.2 K km s^{-1}

the main region of emission is found between the center and the eastern portion of the map.

3.3. $C^{18}O(1–0)$

The C^{18}O spectra have simple profiles, with only a single velocity component, and are narrow. The emission originates from a very well defined region associated with the IRAS source, as one can see in Fig. 4, where a map of the total integrated intensity in the C^{18}O(1–0) line is shown. We note that the emission is mostly coming from a region elongated from SW to NE. Its peak velocity (~ 3 km s^{-1}) is approximately coincident with that of C^{32}S, C^{34}S and of the "main" component in the ^{13}CO(1–0) and ^{13}CO(2–1) spectra. No C^{18}O counterpart is seen at the velocity of the ^{13}CO(1–0) "compact" component ($V_{LSR} \simeq 1$ km s^{-1}), above a 3σ limit of 0.09 K (in antenna temperature units). This is not surprising, because the small optical depth of the ^{13}CO(1–0) line at this velocity (see Sects. 4.2 and 6.2) implies a C^{18}O(1–0) opacity < 0.06.

Another interesting feature of the C^{18}O map is the presence of a velocity shift, shown in Fig. 5. The velocity separation between the blue and red lobes in the map is less than 1 km s^{-1}. If the shift is due to a bipolar outflow, then its axis must be almost perpendicular to the line of sight. In Fig. 1 the blue-shifted portion of the line wing extends up to about 2 km s^{-1}, whereas the red-shifted wing is visible up to a maximum of
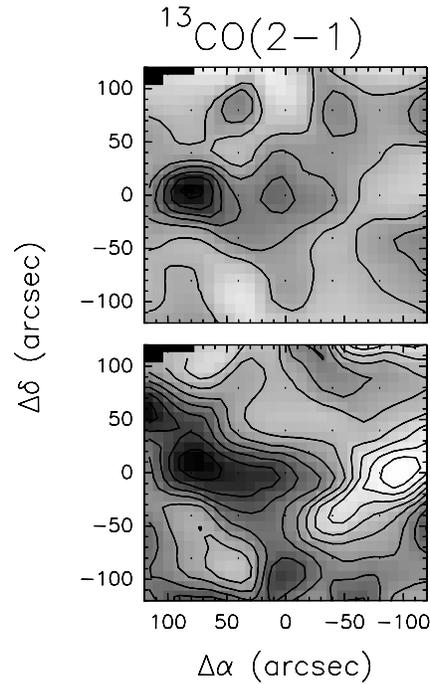
4.8 km s^{-1}. To rule out the possibility that the observed wings could be an instrumental effect, we checked the C^{18}O spectrum against a high SNR C^{34}S spectrum, with the same nominal V_{LSR}: the latter does not show either of the wings detected in the C^{18}O(1–0) spectrum, so that we can conclude that the C^{18}O wings are real.

3.4. $C^{32}S(2–1)$ and $C^{34}S(2–1)$

C^{32}S and C^{34}S are known to be good density tracers. We thus observed the (2–1) transitions of both isotopomers towards the position of I12553. In both cases, we detect the ~ 3 km s^{-1} component, but no emission is visible for ~ 1 km s^{-1}, at the 3σ RMS level. This result is consistent with optically thin emission for $V_{LSR} \simeq 1$ km s^{-1}. The parameters of the C^{32}S and C^{34}S lines obtained by Gaussian fitting are listed in Table 2.

4. Overview of the cloud components and their main physical parameters

4.1. Definition of the main cloud components observed

The detection of a velocity shift across the source in the C^{18}O(1–0) line led us to re-analyze the line-shapes of the ^{13}CO(1–0) observations of OFP. On a careful inspection, the 3 km s^{-1} component in the ^{13}CO(1–0) spectra appears to have in most cases a non-Gaussian profile that changes with position. Two examples
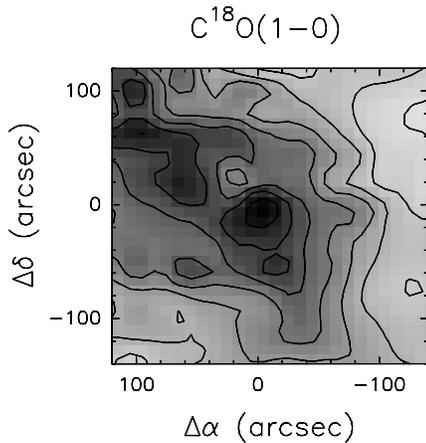
C^{18}O(1–0)

Fig. 4. Map of the integrated C^{18}O(1–0) antenna temperature, from 2.2 to 4.9 km s^{-1}. Contour levels are 0.3 to 3.0 by 0.2 K km s^{-1}

C^{18}O(1–0)

Fig. 5. *Top*: map of the integrated C^{18}O(1–0) antenna temperature, from 2.2 to 2.9 km s^{-1}. Contour levels are 20%, 40%, 60% (dashed line) and 80% of the maximum. The black dots indicate the positions where data were taken. *Bottom*: same as above for the velocity range 3.4 to 4.0 km s^{-1}. Contour levels are 20%, 40%, 60% (dashed line) and 70% of the maximum

of this are the spectra shown in Fig. 6 (see also Fig. 12), which were obtained by averaging four spectra at (-100,100), where the asymmetry is on the blue side, with respect to the peak, and three spectra at (120,80) where the asymmetry is instead on the red side – hereafter (RA,DEC) offsets are assumed to be in seconds of arc.

This suggests that a *three*-component Gaussian decomposition is needed to fit the ^{13}CO(1–0) profiles (even though the choice of the decomposition remains somewhat arbitrary), rather than the two-component used by OFP.

Such components are as follows:

(i) the "main" component of ^{13}CO(1–0) and (2–1) at $V_{\rm LSR} \simeq$ 3 km s^{-1}, detected in all lines observed, including C^{18}O: the latter is characterised by a velocity shift *not* detected in any of the other transitions, which might trace a molecular outflow (Sect. 6); we believe this is the component associated with the IRAS source;

(ii) the "compact" molecular clump, observed mainly in the ^{13}CO(1–0) line, and located close ($\sim 40''$) to the position of I12553, but at $V_{\rm LSR} \simeq 1$ km s^{-1}: we think that this is an isolated clump, *not* associated with the IRAS source (Sect. 5);

(iii) a "drifting" component seen in ^{13}CO(1–0) and, to a lesser extent, in ^{13}CO(2–1), which changes its velocity ($\sim$ 2-4 km s^{-1}) with position: this could be due to the interaction of the outflowing gas with the surrounding molecular cloud (Sect. 7). Fig. 7 shows the smooth velocity drift of the radial velocity of this component, as obtained after a three-component Gaussian fit to the spatially averaged ^{13}CO(1–0) spectra.

In Table 3 we summarize the different components and the molecular tracers in which they are detected.

4.2. Excitation temperature

The physical parameters of the molecular region around I12553 can be estimated by using the procedures outlined in OFP. In particular, one can derive the excitation temperature, $T_{\rm ex}$, from
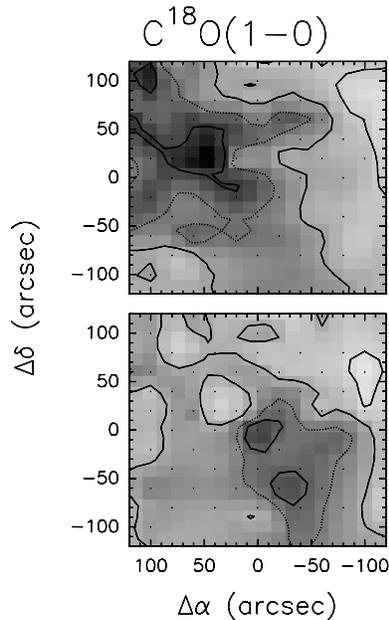
the peak $T_{\rm MB}$ of both ^{12}CO(1–0) and ^{12}CO(2–1) (at $V_{\rm LSR} \simeq$ 3.3 km s^{-1}), where the emission is certainly optically thick. In this way we find an average $T_{\rm ex} \simeq 10.6 \pm 0.3$ K.

Further, having observed both ^{12}CO and ^{13}CO, we can estimate the optical depth assuming the same filling factor and $T_{\rm ex}$ for both species and using the relation (for the same $J \to J - 1$ transition of both ^{12}CO and ^{13}CO):

$$R_{\rm T} \equiv \frac{T_{\rm a}^*(^{12}{\rm CO})}{T_{\rm a}^*(^{13}{\rm CO})} \simeq \frac{T_{\rm MB}(^{12}{\rm CO})}{T_{\rm MB}(^{13}{\rm CO})} \simeq \frac{1 - \exp(-\tau_{13}\, X_{12/13})}{1 - \exp(-\tau_{13})} \quad (1)$$

In Eq. (1) τ_{13} is the ^{13}CO optical depth, and the ^{12}CO optical depth is thus $\tau_{12} = \tau_{13}\, X_{12/13}$, where $X_{12/13} \equiv [^{12}{\rm CO}]/[^{13}{\rm CO}]$ is the isotopic abundance ratio, which we assume to be equal to the terrestrial value, i.e. ~ 89.

As a consistency check, the excitation temperature can be derived from the ratio between the ^{13}CO optical depths in the $J = 1 - 0$ and $J = 2 - 1$ lines (Plambeck et al. 1983): this yields $T_{\rm ex}(^{13}{\rm CO}) \simeq 5 \pm 1$ K, lower than the value found for ^{12}CO.

The inconsistency between $T_{\rm ex}(^{12}{\rm CO})$ and $T_{\rm ex}(^{13}{\rm CO})$ can arise from: (i) differences between the intensity calibration of the 1993 (OFP) and 1995 data (this paper); (ii) an intrinsic difference in temperature at various depths into the cloud, as the ^{13}CO emission could be produced in a colder, inner region, highlighting the problem of using ^{12}CO as a temperature tracer of the entire cloud (Castets et al. 1990); (iii) subthermal excitation of the rarer CO isotopomers; and (iv) our assumption of equal $T_{\rm ex}$ for the ^{13}CO(1–0) and (2–1) transitions.
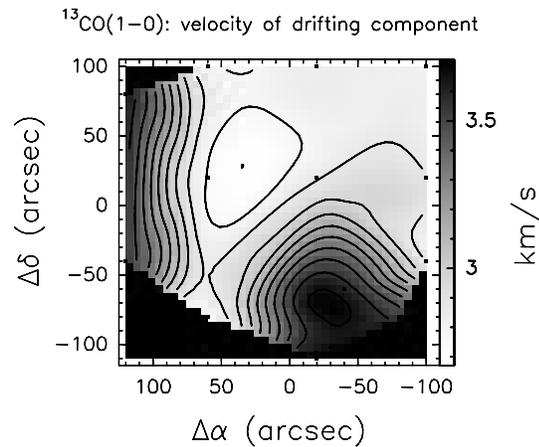
Table 3. Main features of each of the three cloud components as observed in the different molecular tracers

Transition	Compact 1.3 km s^{-1}	Main 3.3 km s^{-1}	Drifting 2-4 km s^{-1}
^{12}CO(2–1)	Clump shifted $\sim 40''$ towards E	Diffuse emission	Not observable
^{13}CO(1–0)[a]	Clump elongated E-W on I12553	Diffuse emission	Variable emission (in intensity and V_{LSR}) with position
^{13}CO(2–1)	Clump shifted $\sim 80''$ towards E	Irregular emission	Not observable
C^{18}O(1–0)	Not detected	Emission orientated NE-SW passing through I12553	Not observable
C^{32}S(2–1)[a]	Not detected	Main clump shifted $\sim 80''$ towards NE	Not observable
C^{34}S(2–1)	Not detected	Emission detected towards I12553	Not observable

[a] From OFP
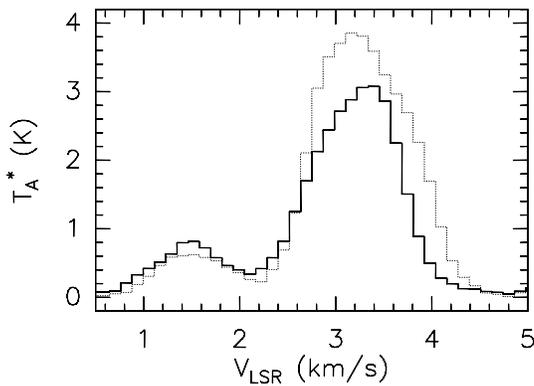
Fig. 6. ^{13}CO(1–0) spectra at position (–100,100) (solid line) and (120,80) (dotted line) resulting from the spatial averaging process described in the text. The change of asymmetry in the line shape is visible at the two opposite positions

Fig. 7. Spatial distribution of the radial velocity of the "drifting" component, as obtained after a three-component Gaussian fit to the spatially averaged ^{13}CO(1–0) spectra. The black dots show the positions around which the spectra have been averaged. The lowest contour level is 2.67 km s^{-1}, and the interval between adjacent contours is 0.1 km s^{-1}

An estimate of the excitation temperature can also be derived from the ^{13}CO emission if this line is optically thick, as suggested by the large ratio $T_a^*(^{13}CO)/T_a^*(^{12}CO) \simeq 0.74$-0.86 at $V_{LSR} = 3.2$ km s^{-1} in the $J = 1 - 0$ transitions towards the central positions. For example, at position (0,0) we obtain $T_{ex}(^{13}CO[1 - 0]) \simeq T_{ex}(^{13}CO[2 - 1]) \simeq 8.6$ K at $V_{LSR} = 3.2$ km s^{-1}, which seems to preclude points (i) and (iv) above, but leaves all the other issues open.

Therefore, we shall assume throughout the rest of this work that $T_k \simeq T_{ex}(^{12}CO) \simeq 10$ K, and take $T_{ex} \simeq 5$-6 K as a lower limit.

5. The "compact" molecular clump at $V_{LSR} \simeq 1$ km s^{-1}

5.1. Identification

OFP observed an elliptical ^{13}CO(1–0) molecular cloud, in the velocity range 0.35-2 km s^{-1}, close to the position of I12553, with its main axis slightly tilted in the NW-SE direction and a morphology suggesting double-peak structure. Their conclusion was that this component was associated with the IRAS
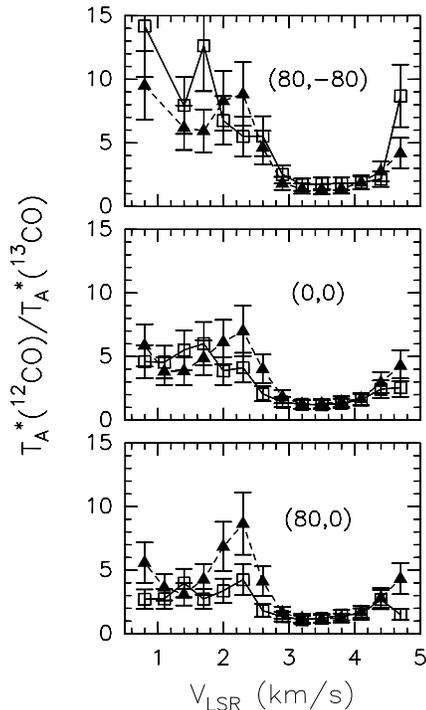
Fig. 8. ^{12}CO/^{13}CO intensity ratios as a function of velocity, at three different positions, as shown at the top right corners of the plots. Filled triangles correspond to the (1–0) transitions, whereas the open squares represent the results for the (2–1) transitions

source. Instead, on the basis of the present work we come to the opposite conclusion, as we are going to show in the following.

First of all, we notice (see Fig. 2 top) that the low velocity ^{12}CO(2–1) emission ($V_{LSR} \lesssim 2.0$ km s^{-1}) does not have its peak at the map center, but at an offset of $\sim 40''$ (0.035 pc) to the east. A similar conclusion holds for the ^{13}CO(2–1) map (Fig. 3 top).

Furthermore, the ^{12}CO to ^{13}CO ratio of antenna temperatures (Fig. 8) can be used to show that the optical depths of the $J = 1 - 0$ and $J = 2 - 1$ transitions of ^{12}CO decrease from ~ 10 to ~ 3 going from $V_{LSR} \simeq 2$-4.5 km s^{-1} to $V_{LSR} \simeq 1.5$-2 km s^{-1}. Such trend is clearly confirmed by our observations in the C^{18}O, CS, and C^{34}S lines, which are not detected at $V_{LSR} \simeq 1$ km s^{-1}.

We conclude that the compact component is an optically thin cloud-component, offset by at least $40''$ from I12553 and hence not associated with it.

5.2. Mass and size

In order to estimate the mass of the compact component, we shall use the ^{13}CO(1–0) observations as the ^{12}CO(2–1) "compact" emission is partly confused by the extended emission.

An important feature of the "compact" ^{13}CO(1–0) is its double-peaked structure in the integrated intensity map, and the small angular displacement between the positions of the blue and red peaks (see Fig. 8 of OFP). If such velocity offset

(0.7-0.9 km s^{-1}) and distance between the peaks (70''-100'', i.e. 0.06-0.085 pc) is interpreted as a rotating disk seen edge-on, the "dynamical mass" turns out to be $\sim$ 1-2 $M_\odot$. Note that if a PMS object is embedded within the molecular clump, this estimate is an upper limit to the disk mass.

Here we question whether such estimate is consistent with the upper limit which one can obtain from the 1.3 mm continuum flux measured by Henning et al. (1993) and with the mass estimated from the ^{13}CO(1–0) line emission.

Henning et al. (1993) give an upper limit to the 1.3 mm continuum emission of 50 mJy in their $23''$ beam centred on the I12553 position. By assuming $T_{ex} \simeq 10$ K and applying Eq. (A10a) of Mezger et al. 1992 with $b = 2.2$ and solar metallicity, one calculates an upper limit to the gas mass of 0.16 $M_\odot$, within the 1.3 mm beam. We stress that such result is not in contradiction with the previous dynamical estimate of $\sim$ 1-2 $M_\odot$, because it refers to a region at least 3 times smaller than the "compact" component. Moreover, the Henning et al. (1993) measurement refers to the I12553 position, whereas the peak of the compact component is offset by $\gtrsim 40''$ to the east. Note also that *a priori* all components contribute to the continuum emission and it is impossible to separate the contribution of the compact component from the others. We thus conclude that the 1.3 mm continuum cannot be reliably used to set an upper limit to the mass of the compact component.

A much better probe of such mass is instead the ^{13}CO(1–0) emission. One can calculate the column density assuming LTE with $T_{ex} = 10$ K and optically thin emission in the line (see e.g. Lis & Goldsmith 1991), and a ^{13}CO abundance relative to H$_2$ of $1.1 \ 10^{-6}$. In order to get the contribution of the compact component *alone*, we have performed the integration in the velocity range 0.35-2.0 km s^{-1}. The column density was then corrected for the finite optical depth of the ^{13}CO(1–0) line, τ_{13}, by multiplying it by $\tau_{13}/[1 - \exp(-\tau_{13})]$ (see OFP and also Frerking et al. 1982). Finally, the total mass was obtained integrating over the area of the compact component. The result is $\simeq 1 \ M_\odot$, consistent with the dynamical estimate.

Incidentally, we note that if one performs the previous integration in the whole velocity range (thus including all the different components) and over a beam area centred on the I12553 position, the resulting mass is 0.18 $M_\odot$, perfectly consistent with the upper limit previously derived from the 1.3 mm continuum flux.

One can reasonably conclude that the mass of the compact component amounts to $\sim$ 1-2 $M_\odot$. However, the data available are not sufficient to confirm the rotating disk hypothesis.

6. The "main" component at $V_{LSR} \simeq 3$ km s^{-1} and the bipolar outflow

6.1. The evidence

As already pointed out in Sect. 5.1, we believe that the compact component is not associated with I12553. Instead, such association does exist with the main component. In fact, as shown in Fig. 4, the C^{18}O emission has only one velocity component

(at $V_{LSR} \simeq 3$ km s^{-1}) that peaks at the position of I12553; unlike the ~ 1 km s^{-1} component, this is also detected in CS and C^{34}S, which is a clear indication of optical tickness of the emitting cloud around I12553. The fact that the emission in the other CO lines is seen on a much larger region than that outlined by the C^{18}O emission is due to optically thick foreground material. This conclusion is also consistent with the large optical depth (~ 10) measured at $V_{LSR} \simeq 3$ km s^{-1} from the ratio between ^{12}CO and ^{13}CO (see Sect. 5.1).

An important feature revealed by the C^{18}O(1–0) maps is the velocity shift shown in Fig. 5. Two main questions arise at this point: is this a bipolar outflow and, if so, why does it *not* show up in the other CO isotopomers? Arguments in favour of a bipolar outflow are:

  (i) the two-lobes morphology;
 (ii) the fact that these lobes seem to "originate" from I12553 (see Fig. 4);
(iii) the detection of line wings in a high SNR spectrum of C^{18}O(1–0);
(iv) the relatively large mechanical energy of the flowing gas, that rules out an interpretation in terms of a gravitationally bound (and rotating) molecular clump (see Sect. 6.3).

All these features suggest that the measured velocity shift traces an outflow, rather than some rotating structure, or a group of clumps with different velocities. If we are observing an outflow, the velocity difference between the emission in the wings and that from the core of the line is very small ($\sim$ 1-1.5 km s^{-1}) compared to other outflows described in the literature (e.g., Haschick 1985, Margulis & Lada 1985). This means that it is either a low-velocity outflow, or that it is seen almost face-on.

However, why is the high velocity gas observable only in the C^{18}O(1–0) transition? We have searched for high velocity wings in ^{12}CO(1–0), ^{12}CO(2–1), ^{13}CO(1–0) and ^{13}CO(2–1), unsuccessfully. We suspect this is because the weaker and possibly optically thin emission of the hypothetic outflow is masked by the diffuse ^{12}CO emission of the ambient molecular gas, whose velocity range exceeds the line wings shown in C^{18}O(1–0) (see Fig. 1). In the case of the ^{13}CO(1–0), all components ("main", "compact", and "drifting") can contribute at masking the outflow. In addition, the ^{13}CO(2–1) spectra have a low SNR and the line wings – if any – are likely to be too weak to be seen in our observations.

On the other hand, the C^{18}O is thin enough to let us see much deeper into the cloud. Furthermore, the contribution of the ambient C^{18}O to the overall emission is limited to a much narrower velocity range, i.e. about 0.8 km s^{-1} compared to $\sim$ 1.4 km s^{-1} and $\sim$ 4 km s^{-1} for ^{13}CO and ^{12}CO, respectively.

6.2. Abundance ratio and optical depth

6.2.1. ^{13}CO to C^{18}O ratio

A basic limitation to the determination of the ^{13}CO to C^{18}O abundance ratio as a function of velocity is the low SNR in the ^{13}CO and C^{18}O (with the single exception of the central [0,0]
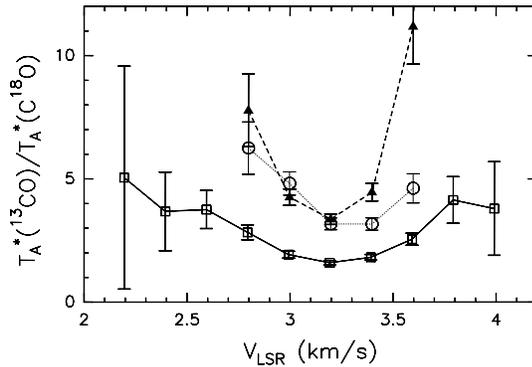

Fig. 9. ^{13}CO(1–0)/C^{18}O(1–0) intensity ratios, as a function of velocity, at three different positions. Open squares and solid line refer to position (0,0), filled triangles and dashed line correspond to position (280,160), and open stars and dotted line refer to position ($-200, -120$)

position) spectra. For this reason we have evaluated the abundance from the ratio of the antenna temperature not corrected for saturation, denoted $R_T \equiv T_a^*(^{13}CO[1\text{-}0])/T_a^*(C^{18}O[1\text{-}0])$ (not to be confused with the R_T used in Sect. 4.2), and also from the ratio of the integrated line intensities, denoted by $R_I \equiv \int T_a^*(^{13}CO)\,dv / \int T_a^*(C^{18}O)\,dv$.

R_I at an off-center position, where both lines are assumed optically thin, provides the ^{13}CO to C^{18}O abundance ratio, $X_{13/18}$. The profile averaged optical depth of ^{13}CO is obtained at the (0,0) position with an equation similar to Eq. (1). Using $R_I = 6.0$ calculated at position (-200,-120) as an estimate of $X_{13/18} \equiv [^{13}CO]/[C^{18}O]$, one derives a profile-averaged ^{13}CO optical depth $\tau_{13} \simeq 2.4$ at position (0,0), where $R_I = 2.3$.

We have then evaluated R_T at these two positions and also at position (280,160), as shown in Fig. 9. We note four main features: (i) At positions (0,0) and ($-200, -120$) R_T rises in the line wings. (ii) This increase is more significant at position ($-200, -120$), which is probably suggesting that even far from the nominal position of I12553 the central velocity range of the lines must still correspond to partially optically thick cloud components, whereas the line wings begin to represent emission from presumably optically thin components (see Langer et al. 1989). However, our signal-to-noise ratio in these wings is not high enough to determine any limiting value to R_T at higher velocities (see Lis & Goldsmith 1991). (iii) The R_T values measured in the line wings at the central position (0,0) are fairly close to the ratios observed at the line center of position (-200,-120), and are also consistent with the $X_{13/18}$ estimates obtained by using R_I. Furthermore, position (280,160) is an example of a location in the cloud where the apparent line saturation is smaller. (iv) The differences observed in the [^{13}CO]/[C^{18}O] ratios at various positions may also indicate some source of enhancement of the ^{13}CO emission in the outer parts of the cloud, for example by means of chemical fractionation of ^{13}C (Langer et al. 1980).
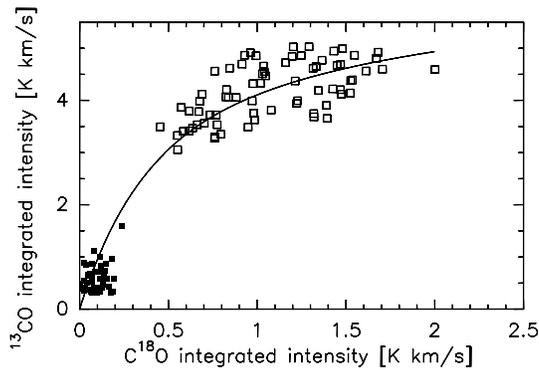
Fig. 10. Integrated $C^{18}O(1-0)$ intensity plotted as a function of integrated $^{13}CO(1-0)$ intensity. The velocity interval used for the integration is 2.3 to 4.3 km s^{-1} (open squares), and integrated intensities > 0.3 K km s^{-1} only are plotted. Our data lie only in the saturated part of the plot, and the solid line represents the fit to the data (see text). Also shown are lower limits obtained using the velocity interval 3.8 to 4.8 km s^{-1} (filled squares)

6.2.2. Curve of growth analysis

As an alternative approach to the calculation of $[^{13}CO]/[C^{18}O]$, we have also applied a curve of growth analysis to our data (see Spitzer 1968 and his Eq. [2-38]). The $C^{18}O$ and – assuming a certain value for $[^{13}CO]/[C^{18}O]$ – the ^{13}CO optical depths are calculated. We then compare the observed ^{13}CO integrated emission with that calculated using the formulae of Spitzer, adequately modified for use with radioastronomical quantities. The excitation temperature and the abundance are changed until a χ^2 is minimized.

In Fig. 10 we thus plot the integrated $^{13}CO(1-0)$ emission as a function of $C^{18}O(1-0)$ integrated emission. The best fit to the data yields $[^{13}CO]/[C^{18}O]= 7.7^{+0.7}_{-1.3}$ and $T_{ex} = 5.5 \pm 0.5$ K, and is shown by the solid line in Fig. 10. We also note that the observed data points are not in the linear part of the curve of growth, which suggests a widespread, partially thick ^{13}CO.

In Fig. 10 we also plot the points corresponding to the lower limits obtained for the high velocity redshifted gas, between 3.8 and 4.8 km s^{-1}. Most of these fall below the fit of the curve of growth: such result justifies why the wings are not detected in the $^{13}CO(1-0)$ line. We stress that the lower limits were not used in the fit shown in Fig. 10.

Hence the derived abundance is consistent, although somewhat higher, with the estimates obtained using the R_I and R_T ratios, as discussed above. This is not surprising since, as we mentioned above, the R_I and R_T ratios we used are not corrected for saturation effects. The excitation temperature is however less than $T_{ex}(^{12}CO)$, yet it is consistent with the lower limit obtained using ^{13}CO (Sect. 4.2).

6.3. Other physical parameters

An estimate of the H$_2$ density in the "main" component can be obtained from the $C^{32}S$ and $C^{34}S(2-1)$ lines. We assume that the CS clump is resolved in both transitions, as the $C^{32}S$ map

of OFP seems to indicate. One can then compute the brightness temperature of the lines by solving the statistical equilibrium equations under the large-velocity-gradient approximation (see e.g. Cesaroni et al. 1991). In particular, the ratio between the two lines (i.e. the optical depth) depends on density and kinetic temperature: if one assumes that the kinetic temperature is the same as the T_{ex} derived from the CO lines (10 K), the observed ratio corresponds to a density of $(7 \pm 3) \, 10^5$ cm^{-3}, allowing for a 15% uncertainty on each line.

As far as the outflow is concerned, the column density in the $C^{18}O$ line wings and the outflow total mass, M_{flow}, can be derived. Assuming $T_{ex} \simeq 10$ K and integrating from 1.8 to 2.9 km s^{-1} for the blue-wing and from 3.5 to 4.8 km s^{-1} for the red one, we find a hydrogen mass for the *outflowing* gas of about 2.9 $M_\odot$, whereas the mass of the gas associated with the "core" emission is about 5.7 $M_\odot$. The total $C^{18}O$ column density is $5.9 \, 10^{14}$ cm^{-2}, $3.7 \, 10^{14}$ cm^{-2} and $1.4 \, 10^{15}$ cm^{-2}, for the blue-shifted, red-shifted and bulk gas, respectively. Estimates of outflow momenta and energies are more uncertain because only the velocity component along the line of sight is measured, and also because it depends on the method or assumptions used to carry out the integrations over velocity and position (for a full discussion see, e.g., Lada 1985 and Cabrit & Bertout 1986).

Here, we shall assume that the outflow is a constant velocity flow with velocity $V_{max} \simeq 1.6$ km s^{-1} (also, no projection effects will be considered here). As pointed out in Lada (1985), this particular choice of V gives an upper limit to the momentum and the kinetic energy of the flow. The outflow momentum, is $p_{flow} = M_{flow} V_{max} = 4.7 \, M_\odot$ km s^{-1}, and the kinetic energy $E_{flow} = M_{flow} V_{max}^2/2 = 7.4 \, 10^{43}$ erg. This energy is much larger than the gravitational binding energy ($\sim 3 \, 10^{42}$ erg) of the gas, and hence the gas seen in the $C^{18}O$ wings is very unlikely to be self-bound.

6.4. Luminosity and dynamical time-scale

The observed maximum outflow radius, $R_{flow} = 0.175$ pc, coupled with V_{max} can be used to get the dynamical time-scale of the flow, $t_d = R_{flow}/V_{max} \simeq 1.1 \, 10^5$ yrs. This is very uncertain, not only because of the unknown inclination angle (as R_{flow} is the *projected* size, and V_{max} is a *radial* velocity), but also because the physical extent of an outflow is affected by the surrounding molecular cloud. The mechanical luminosity of the flow is $L_{flow} = E_{flow}/t_d = 5.6 \, 10^{-3} \, L_\odot$. As for most known outflows, the bolometric luminosity, $L_\star$, of the central source (1.2 $L_\odot$) is larger than the mechanical luminosity, and the ratio $L_{flow}/L_\star = 4.7 \, 10^{-3}$ indicates a relatively efficient conversion from radiant to mechanical energy.

We cannot obtain a direct estimate of the mass of the central star in I12553. However, we still can get some useful insights if we assume a spherically symmetric collapse. In fact, in this case the accretion luminosity is (Shu et al. 1987):

$$L_{acc} = \frac{G \, M_\star \, \dot{M}_{acc}}{R_\star} \tag{2}$$

where the mass accretion rate can be derived from:

$$\dot{M}_{\mathrm{acc}} = 0.975 \frac{a^3}{G} = 2\,10^{-6} \left(\frac{T_{\mathrm{k}}}{10\,\mathrm{K}}\right)^{1.5} M_\odot\,\mathrm{yr}^{-1} \tag{3}$$

with a isothermal sound speed and $T_{\mathrm{k}} \simeq 10$ K.

From Basri & Bertout (1989) we find that in their limited sample of T Tauri stars (TTS), $0.03 \lesssim L_{\mathrm{acc}}/L_\star \lesssim 2.1$. If we now derive $\dot{M}_{\mathrm{acc}}$ from Eq. (3) (spherical accretion) and assume $L_{\mathrm{acc}} \simeq L_{\mathrm{flow}}$, then utilising Eq. (2) one can write the following limits for the $M_\star/R_\star$ ratio:

$$5.8\,10^{-4} \lesssim \frac{M_\star}{R_\star} \lesssim 0.04 \quad M_\odot\,R_\odot^{-1} \tag{4}$$

which is much lower than the range, $M_\star/R_\star \simeq 0.1\text{–}1\,M_\odot\,R_\odot^{-1}$, quoted by Basri & Bertout (1989).

Therefore, even if the kinetic temperature of the gas were lower (using the lower limit on T_{k} of about 5 K leads to $1.7\,10^{-3} \lesssim M_\star/R_\star \lesssim 0.1\,M_\odot\,R_\odot^{-1}$), the estimated $M_\star/R_\star$ ratio suggests that I12553 is in a somewhat earlier phase than a TTS. This is in fact consistent with the IRAS colors of I12553, as stated in Sect. 1. However, In the case of accretion through a disk much lower accretion rates should be used ($\dot{M}_{\mathrm{acc}} \simeq 10^{-8} - 10^{-7}\,M_\odot\,\mathrm{yr}^{-1}$), which would increase the $M_\star/R_\star$ ratio.

7. The drifting component and the interaction of the outflow with the ambient gas

Though more sensitive, higher spatial resolution observations are needed to confirm the $C^{18}O$ bipolar outflow interpretation, we now consider the observational consequences of the interaction of the outflow with the surrounding medium. In particular, we shall show that a model in which the bipolar outflow interacts with the ambient gas (mainly traced by ^{13}CO), is consistent with the observational data. We shall show that the ambient gas may be accelerated as a consequence of this interaction, giving rise to the observed deviations from Gaussian shape for the ^{13}CO line profiles (see Fig. 6).

7.1. Energy requirements

Before describing the model, we want first to check that the energy in the outflowing gas can account for the acceleration of the ambient gas.

The energy required to accelerate the gas of mass M_{g} to the velocity $V_{\mathrm{drift}} - V_{\mathrm{bulk}}$ is

$$W = \frac{M_{\mathrm{g}}\,(V_{\mathrm{drift}} - V_{\mathrm{bulk}})^2}{2(\sin^2 \alpha)} \tag{5}$$

where V_{bulk} is the bulk velocity of the ambient gas (see next section) and V_{drift} is the velocity of the accelerated gas that we have previously called the "drifting" component (see Sect. 4.1), both measured along the line of sight. The angle α is the angle between the line of sight and the direction of the outflow (see Fig. 11).

To calculate M_{g} we have used the method outlined in Sect. 5.2 applied to all those positions where a "bump" is seen in the $^{13}CO(1\text{–}0)$ spectra. We thus obtain $M_{\mathrm{g}} \simeq 1.7\,M_\odot$ and, given a typical value of $(V_{\mathrm{drift}} - V_{\mathrm{bulk}})^2 \simeq 0.16\,\mathrm{km}^2\,\mathrm{s}^{-2}$, we finally get $(\sin^2 \alpha)\,W \simeq 2.7\,10^{42}$ erg, which is comparable to the total energy associated with the molecular outflow $E_{\mathrm{flow}} = 7.4\,10^{43}$ erg.

7.2. A simple model

In Fig. 11 we present a two-dimensional cut of our model, where the central source of energy (indicated with O), two parallel slabs of molecular gas, and two reference frames are shown.

In our simple model a bipolar outflow is ejected from the central source and propagates in the plane of the top portion of Fig. 11, which shows the direction of the outflow approaching the observer. This propagation occurs first in an hollow cavity, until it strikes two slabs of gas. Only the slab on the same side as the observer is shown in Fig. 11. The gas in this slab, located at the interface with the outflowing material, is accelerated along the length of the slab itself up to a maximum excess velocity V_{exc}. It returns back to its systemic velocity, V_{bulk}, only at a certain distance from the region of interaction. This interface region is then followed by the ambient gas which contributes to the emission at the systemic velocity.

The interested reader will find further details on this model, and the derivation of the $^{13}CO(1\text{–}0)$ line brightness temperature, in the appendix. Here, we list the main assumptions of the model:

- The gas in the first slab, of thickness S_{slab}, is accelerated only in the y' direction, i.e. parallel to the walls of the slabs.
- The outflow is perpendicular to the plane of interaction at all points on the line passing through P and parallel to z.
- The gas struck by the outflowing material will experience the same acceleration in all planes parallel to the $x'y'$ plane (equivalent to the independence of the acceleration from $z' = z$). We shall also assume that the acceleration experienced by the gas in the first slab is independent of x'.
- The velocity of the gas in the first slab, after the initial acceleration caused by the interaction with the outflow, returns to the bulk velocity of the ambient gas (i.e., the velocity assigned to the foreground slab) at a distance y'_{max}, measured along the y' axis.

The consistency of this model with the data can be tested by reproducing the $^{13}CO(1\text{–}0)$ line profiles at three different positions in the cloud, in which the blue- and red-shifted asymmetries of the line profile are more evident.

To do this, we first averaged the spectra around positions $(-100, 100)$ (four spectra) and $(-20, -120)$ (two spectra) where the asymmetry is clearly on opposite sides with respect to the main component, and around $(-60, -20)$ (four spectra). We will refer to these three positions, and the corresponding spectra, with the letters A, B and C, respectively. The parameters of the fit performed using Eqs. (A1) to (A4) have been kept constant for the three positions, with the only exceptions being explained in the appendix. The model profiles (Fig. 12) show that the shape of the asymmetry in the line profile can be correctly reproduced.
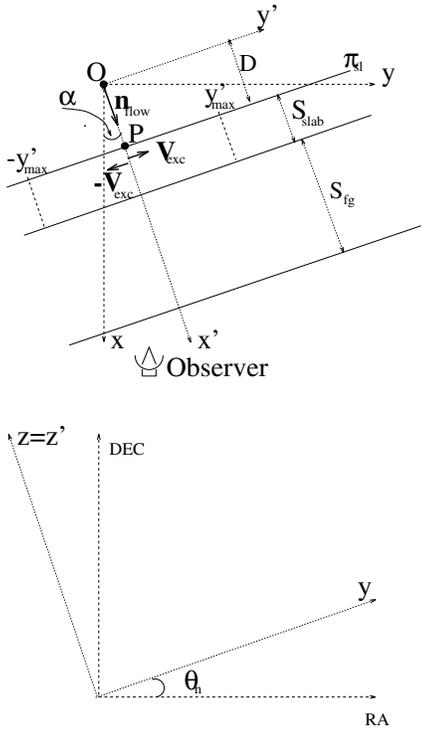
Fig. 11. Schematic representation of the model described in the text, in a reference frame co-moving with the ambient gas. *Top*: the coordinate system seen from $z = +\infty$: the plane of the figure is perpendicular to the planes delimiting the two slabs of gas. *Bottom*: front view, with the line of sight perpendicular to the plane of the figure

We conclude that even if the model is very crude, it is nevertheless able to *qualitatively* explain the observed asymmetry of the ^{13}CO line profiles.

8. Conclusions

The molecular gas surrounding the PMS candidate I12553 in the Chamaeleon II cloud has been studied using several mm-wave rotational transitions of CO, CS and their isotopomers. These new observations have considerably improved the scenario previously discussed by OFP. Five main facts have emerged from the analysis of the observations:

1. On the basis of all transitions observed, three different components are identified in the region: the "main" component at $V_{LSR} \simeq 3$ km s^{-1}, a "compact" clump at $V_{LSR} \simeq 1$ km s^{-1}, and a "drifting" component with V_{LSR} varying over the range 2-4 km s^{-1}.
2. The "compact" component is an isolated clump probably *not* associated with the IRAS source, and which can be barely seen in the ^{12}CO(2–1) map.
3. The "main" component is detected in high density gas ($[7 \pm 3] 10^5$ cm^{-3}) at the position of I12553 at $V_{LSR} \simeq 3$ km s^{-1} through the CS transitions. Also, C^{18}O observations show that this molecular gas is tracing a dense clump where the IRAS source has formed.
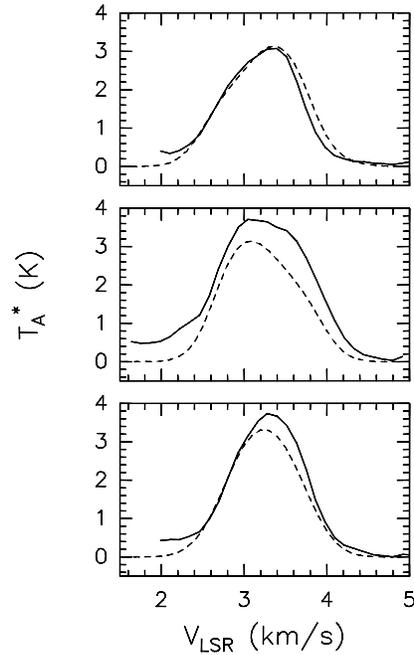

Fig. 12. *Top*: observed spectrum (solid line) at position $(-100, 100)$ with superimposed the model profile (dashed line). *Middle*: the same at position $(-20, -120)$. *Bottom*: the same at position $(-60, -20)$. For $V_{LSR} \lesssim 2.4$ km s^{-1} the observed profiles are affected by the component at $V_{LSR} \simeq 1$ km s^{-1}, which is not included in the model

4. The "main" component cannot be identified in the ^{12}CO and ^{13}CO lines because the high optical depths in these transitions prevents separation from the foreground diffuse emission.
5. the C^{18}O(1–0) line at $V_{LSR} \simeq 3$ km s^{-1} shows the presence of a velocity-shift, which we propose to be a bipolar molecular outflow physically associated with the IRAS source. We do *not* detect this velocity shift in the other CO isotopomers, and we ascribe this to the overall optically thick emission of the ambient molecular gas.
6. The "drifting" component can be the consequence of the interaction of the gas outflowing from the embedded IRAS source with the ambient molecular material. A simple model of laminar flow induced in the ambient material qualitatively reproduces the observed asymmetry in the ^{13}CO(1–0) line profiles.
7. The estimated $M_\star/R_\star$ ratio indicates that I12553 is in a somewhat earlier phase than a T Tauri star, as suggested by its IRAS colors.

Appendix A: description of the model reproducing the ^{13}CO(1–0) profiles

We describe here how to derive the ^{13}CO(1–0) line brightness temperature using the model for the interaction between the

outflowing gas from I12553 and the surrounding diffuse gas discussed in Sect. 7 and illustrated in Fig. 11.

Two directions are set: the unit vector lying on the line of sight, or the x axis, and the unit vector parallel to the outflow axis, $\mathbf{n}_{\text{flow}}$. These define a plane which contains the two reference frames shown in Fig. 11. The x' axis is chosen along the outflow direction, i.e. the $\mathbf{n}_{\text{flow}}$ vector. The y and y' axis are then chosen such that the $x'y'$ and xy planes are both coincident and coplanar with the plane defined by $\mathbf{n}_{\text{flow}}$ and and the line of sight. The y axis lies at an angle θ_{n} to the RA axis, while α is the angle between the x and x' axis.

S_{slab} and S_{fg} are the thickness of the slab where the gas is being accelerated (as a consequence of the interaction with the outflow from the source at O) and that of the foreground material, respectively. The planes delimiting these slabs are mutually parallel and perpendicular to the xy (or $x'y'$) plane. The slab containing the ambient molecular gas is assumed to be unaffected by the outflow, and will thus contribute only to the quiescent ^{13}CO emission.

Given the geometrical configuration described above, the brightness temperature along a given line of sight (y, z), at velocity V, is given by:

$$T_{\text{b}}(y, V) = [J_\nu(T_{\text{ex}}) - J_\nu(T_{\text{bg}})] [1 - e^{-\tau(y, V)}] \quad \text{(A1)}$$

where $J_\nu(T) = (h\nu/k)[\exp(h\nu/kT) - 1]^{-1}$ and we have implicitly assumed invariance with respect to z, as explained in Sect. 7.2. The optical depth is given by $\tau(y, V) = \tau_1(y, V) + \tau_2(y, V)$, the sum of the contributions from the first slab, where the gas is accelerated (τ_1), and from the second slab, i.e. the foreground contribution (τ_2), as decribed in Sect. 7. More exactly, $\tau_2(y, V)$ should be interpreted as the sum of the foreground *and* background contributions of the ambient gas; this does not change the validity of the present arguments and formulae. Finally, T_{ex} is the excitation temperature found in Sect. 4.2, and is assumed to be the same everywhere.

We then express each of the $\tau_i(y, V)$ ($i = 1, 2$) in the following way:

$$\tau_i(y, V) = \tau_{\circ i} \int_{x_{\min}}^{x_{\max}} 2 \sqrt{\frac{\ln 2}{\pi}}$$
$$\exp\left[-4 \ln 2 \left(\frac{V - V_{\text{i}}(x, y)}{\Delta V_{\text{i}}}\right)^2\right] dx \quad \text{(A2)}$$

where the dependence on the Gaussian line profile has been explicitly written. $\tau_{\circ i}$ represents the peak optical depth per unit length in each of the slabs, ΔV_{i} is the line full width at half maximum, and $x_{\min}$ and $x_{\max}$ are the points of interception of the line of sight with the planes limiting the two slabs, different for each of them (the i subscript is dropped for the sake of simplicity). $V_{\text{i}}(x, y)$ is the component of the velocity parallel to the line of sight as measured in a reference frame co-moving with the ambient gas, i.e. the gas located in the second slab, which has a bulk velocity along the line of sight V_{bulk}. Therefore

Table 4. Best fit values of V_{exc} and V_{bulk}

Line	V_{exc} (km s^{-1})	V_{bulk} (km s^{-1})
A	0.60	3.30
B	0.60	3.15
C	0.40	3.30

$V_2(x, y) = 0$ in the foreground gas, whereas in the first slab the velocity can be written as:

$$V_1(x, y) = \begin{cases} 0 \\ V_{\text{exc}} \sin \alpha \left| \frac{y'(x, y) - y'_{\max}}{y'_{\max}} \right|^\gamma \\ -V_{\text{exc}} \sin \alpha \left| \frac{y'(x, y) + y'_{\max}}{y'_{\max}} \right|^\gamma \end{cases} \quad \text{(A3)}$$

where the first equality holds for $|y'| \geq y'_{\max}$, the second one holds in the interval $0 < y' < y'_{\max}$ and the third one for $-y'_{\max} < y' < 0$. V_{exc} is the maximum excess velocity, measured along the y' coordinate (the value of which depends upon x and y), of the ambient gas in the first slab, as a consequence of the interaction with the outflow; γ is the (positive) exponent in the power law which determines how quickly the velocity of the accelerated gas returns to its bulk value.

The line profile, i.e. the resulting main-beam brightness temperature as a function of velocity, can then be calculated by integrating the brightness temperature in the y direction over the main beam, and taking into account the bulk velocity of the gas, i.e.:

$$T_{\text{MB}}(V) = \frac{1}{\Omega_{\text{MB}}} \int_{\text{MB}} T_{\text{b}}(y, V) \, d\Omega =$$
$$= \frac{4}{\pi (l_{\text{HPBW}})^2} \int_{y_0 - l_{\text{HPBW}}/2}^{y_0 + l_{\text{HPBW}}/2} T_{\text{b}}(y, V)$$
$$\sqrt{(l_{\text{HPBW}}/2)^2 - (y - y_0)^2} \, dy \quad \text{(A4)}$$

where Ω_{MB} is the solid angle corresponding to the full extension of the main beam, the profile of which has been assumed circular in shape and equal to 1 within Ω_{MB} and 0 outside. Moreover, l_{HPBW} represents the linear distance corresponding to the antenna HPBW at the distance of Cha II, and $y_0 = y_0(\text{RA}, \text{DEC})$ represents a line of sight through the cloud.

The best fits are shown in Fig. 12. These have been obtained with the following input parameters: T_{ex}=10 K, $\alpha = 210$, $D = 0.08$ pc, $S_{\text{slab}} = 0.24$ pc, $S_{\text{fg}} = 0.62$ pc, $\Delta V_1 = 0.6$ km s^{-1}, $\Delta V_2 = 0.8$ km s^{-1}, $\tau_{01} = 2.3$, $\tau_{02} = 1.45$, $\gamma = 1.5$, $y'_{\max} = 2$ pc; V_{exc} and V_{bulk} vary with position, and are listed in Table 4.

References

Basri, G., Bertout, C., 1989, ApJ 341, 340

Booth, R.S., Delgado, G., Hagström, M., et al., 1989, A&A 216, 315

Cabrit, A., Bertout, C., 1986, ApJ 307, 313

Castets, A., Duvert, G., Dutrey, A., Bally, J., Langer, W.D., Wilson, R.W., 1990, A&A 234, 469

Cesaroni, R., Walmsley, C.M., Kömpe, C., Churchwell, E. 1991, A&A, 252, 278 van Dishoeck, E.F., 1989, ApJ 345, 815

Frerking, M.A., Langer, W.D., Wilson, R.W., 1982, ApJ 262, 590

Gregorio Hetem, J.C., Sanzovo, G.C., Lépine, J.R.D., 1988, A&AS 76, 347

Gregorio Hetem, J.C., Sanzovo, G.C., Lépine, J.R.D., 1989, A&AS 79, 452

Haschick, A.D., Editor, "Masers, Molecules and Mass Outflows in Star Forming Regions", Proc. of a meeting held by the Haystack Obs., 15-16 may 1985

Henning, Th., Pfau, W., Zinnecker, H., Prusti, T., 1993, A&A 276, 129

Kutner, M.L., Ulich, B.L., 1981, ApJ 250, 341

Lada, C.J., 1985, ARAA 23, 267

Lada, C.J., 1991, "The Physics of Star Formation and Early Stellar Evolution", C.J. Lada and N.D. Kylafis, editors, Kluwer Ac. Publ., 329

Langer, W.D., Wilson, R.W., Goldsmith, P.F., Beichman, C.A., 1989, ApJ 337, 355

Langer, W.D., Goldsmith, P.F., Carlson, E.R., Wilson, R.W., 1980, ApJ 235, L39

Lis, D.C., Goldsmith, P.F., 1991, ApJ 369, 157 333, 821

Margulis, M., Lada, C.J., 1985, ApJ 299, 925

Mezger, P.G., Sievers, A., Zylka, R., Haslam, C.G.T., Kreysa, E., Lemke, R., 1992, A&A 265, 743

Olmi, L., Felli, M., Prusti, T., 1994, A&A 288, 591 (OFP)

Plambeck, R.L., Snell, R.L., Loren, R.B., 1983, ApJ 266, 321

Prusti, T., Whittet, D.C.B., Assendorp, R., Wesselius, P.R., 1992, A&A 260, 151

Shu, F.H., Adams, F.C., Lizano, S., 1987, ARA&A 25, 23

Spitzer, L., 1968, Diffuse Matter in Space, J. Wiley & Sons, New York

Whittet, D.C.B., Assendorp, R., Prusti, T., Roth, M., Wesselius, P.R., 1991, A&A 251, 524